Effects of coronal mass ejection orientation on its propagation in the heliosphere

K. Martinić[1], M. Dumbović[1], J. Čalogović[1], B. Vršnak[1], N. Al-Haddad[3], and M. Temmer[2]

[1] Hvar Observatory, Faculty of Geodesy, University of Zagreb, Zagreb, Croatia
e-mail: kmartinic@goef.hr
[2] Institute of Physics, University of Graz, Graz, Austria
[3] University of New Hampshire, Space Science Center, Durham, USA

ABSTRACT

Context. In the scope of space weather forecasting, it is crucial to be able to more reliably predict the arrival time, speed, and magnetic field configuration of coronal mass ejections (CMEs). From the time a CME is launched, the dominant factor influencing all of the above is the interaction of the interplanetary CME (ICME) with the ambient plasma and interplanetary magnetic field.
Aims. Due to a generally anisotropic heliosphere, differently oriented ICMEs may interact differently with the ambient plasma and interplanetary magnetic field, even when the initial eruption conditions are similar. For this, we examined the possible link between the orientation of an ICME and its propagation in the heliosphere (up to 1 AU).
Methods. We investigated 31 CME-ICME associations in the period from 1997 to 2018. The CME orientation in the near-Sun environment was determined using an ellipse-fitting technique applied to single-spacecraft data from SOHO/LASCO C2 and C3 coronagraphs. In the near-Earth environment, we obtained the orientation of the corresponding ICME using in situ plasma and magnetic field data. The shock orientation and nonradial flows in the sheath region for differently oriented ICMEs were investigated. In addition, we calculated the ICME transit time to Earth and drag parameter to probe the overall drag force for differently oriented ICMEs. The drag parameter was calculated using the reverse modeling procedure with the drag-based model.
Results. We found a significant difference in nonradial flows for differently oriented ICMEs, whereas a significant difference in drag for differently oriented ICMEs was not found.

Key words. Coronal mass ejection – Inclination – Propagation properties

1. Introduction

A coronal mass ejection (CME) is a large-scale ejection of plasma and magnetic field from the solar corona into the interplanetary medium. When it reaches Earth, it can cause large disturbances in the near-Earth environment (i.e., it can trigger geomagnetic storms). It is relatively widely accepted that CMEs consist of a so-called flux rope (FR) structure (Chen 1996; Bothmer & Schwenn 1998; Moore et al. 2001) that may drive sheaths and shocks. An FR, in its simplest form, is a cylindrical structure in which a poloidal magnetic field component rotates about an axial magnetic field component that follows the central axis of the cylinder (Lundquist 1950).

Coronal mass ejections have been observed remotely with white-light coronagraphs. A CME FR reconstruction can be performed using stereoscopic coronagraph images. Thernisien et al. (2006) developed a 3D model for CME FR reconstruction, referred to as the graduated cylindrical shell (GCS) model, in which an FR is represented as a "hollow croissant" consisting of two conical legs and a curved front. One of the six main parameters to fully describe the FR in the GCS reconstruction is tilt. The tilt of an FR is defined as the angle between the solar equator and the central axis of the FR. It is measured from solar west to solar north (positive values) and from solar west to solar south (negative values). Defined in this way, the tilt essentially gives the inclination of the CME with respect to the solar equator. Another way to determine the inclination of a CME is

based on a 2D CME reconstruction, first proposed by Chen et al. (1997), where the observed CME front is represented with an ellipse. In this model, changing the position of the ellipse, the length of the axes, and the inclination of the major axis of the ellipse can account for the angular width and inclination of the CME (Krall & St. Cyr 2006; Byrne et al. 2009; Martinić et al. 2022). Martinić et al. (2022) showed that GCS and ellipse fitting give comparable results for the inclination of CMEs when using remote data from coronagraphs aboard the SOHO and STEREO spacecraft for 22 Earth-directed events.

Commonly, there is a distinction between the CMEs observed remotely in the corona and the interplanetary CMEs, or ICMEs, measured in situ by spacecraft. Recently, however, in situ measurements of CMEs in the upper corona and innermost heliosphere taken with the Parker Solar Probe and Solar Orbiter have caused this traditional distinction between CMEs and ICMEs to become less clear. In this study, we use the term "ICME" in the context of in situ measurements and interplanetary interaction with the ambient; for the rest, the "CME" term is used.

Typically, the three-part structure (the shock, the sheath, and the magnetic obstacle) can be well-measured as the spacecraft passes an ICME. First, a fast-forward shock front is usually detected, characterized by an abrupt increase in magnetic field, solar wind speed, and temperature. After the shock front, a so-called ICME sheath region is measured. This is a special case of plasma sheaths where both expansion and propagation prop-

erties are observed (Siscoe & Odstrcil 2008). The ICME sheaths are turbulent and compressed, as evidenced by elevated values and strong fluctuations of the magnetic field, density, velocity, and plasma beta parameter (Kilpua et al. 2017). After the sheath is the driver, the FR part of the ICME, that is, the magnetic obstacle (MO). A subset of well-defined MOs is called a magnetic cloud (MC), which is characterized by a smoothly rotating magnetic field, decreased plasma beta parameter, and decreased temperature (Burlaga 1991). As a first approximation, and based on their chirality and orientation, ICMEs can be classified into eight basic types, as described in Bothmer & Schwenn (1998), Mulligan et al. (1998), and recently by Palmerio et al. (2018). Four of these eight types are low-inclined ICMEs, and the remaining four are high-inclined ICMEs.

Three forces are active during different CME propagation phases. In the early acceleration phase, the Lorentz and gravitational forces compete with each other. Later, the magnetohydrodynamic (MHD) drag force from the solar wind acts on the CME. Observations have shown that CMEs faster than the solar wind slow down, while CMEs slower than the solar wind accelerate (Sheeley et al. 1999; Gopalswamy et al. 2000; Vršnak et al. 2004; Manoharan 2006).

Drag in interplanetary space (MHD drag) is not primarily caused by viscosity and particle collisions but is rather related to the interaction of the ICME with the surrounding magnetic field, such as MHD waves (Cargill et al. 1996) and magnetic field draping (Gosling & McComas 1987), as described in Martinić et al. (2022). Interplanetary CMEs interact with the surrounding plasma and magnetic field as they propagate in the heliosphere. For fast ICMEs embedded in the slow ambient plasma, accelerations and deflections of the ambient plasma occur in front of the ICME FR part. Due to the high electrical conductivity, the ambient solar wind cannot easily penetrate the magnetized ICME structure, but it is accelerated and deflected around the obstacle. This occurs in an ICME sheath region and is particularly pronounced near the ICME FR part. A direct consequence of this plasma motion is the draping of the IMF around the ICME FR. Apart from the relative velocity between the ICME and the surrounding solar wind, the draping pattern depends strongly on the size and shape of the ICME and on the configuration of the surrounding magnetic field (Gosling & McComas 1987; McComas et al. 1988; McComas et al. 1989). Consequently, for differently oriented ICMEs, even if embedded in similar configurations of the ambient magnetic field and solar wind, one might expect a different plasma flow and consequently a different draping pattern, as theorized by Martinić et al. (2022). Figure 1 shows a low-inclination ICME in panel (a) and a high-inclination ICME embedded in the surrounding magnetic field in panel (b). Only the meridional plane, the xz-plane of the Geocentric Solar Ecliptic (GSE) coordinate system, is shown in Figure 1, and one should consider the Parker spiral (i.e., the Parker spiral configuration of the magnetic field in the xy-plane). In the case of ICMEs with high inclination, more draping occurs due to the interaction with the broader extent of the ICME front. The blue arrows in Figure 1 schematically represent the plasma flows in front of the obstacle. Due to the larger pressure gradient associated with the pileup of the magnetized solar wind, the ambient plasma is expected to pass the obstacle more easily in the direction in which the extent of the obstacle is smaller. Thus, in an ICME with low inclination, the plasma flow in the xz-plane of the GSE coordinate system is more pronounced than in an ICME with high inclination. In contrast, for an ICME with high inclination, one would expect more pronounced plasma flows in the yz-plane (into and out of the plane shown in Figure 1). The ambient field that is draped
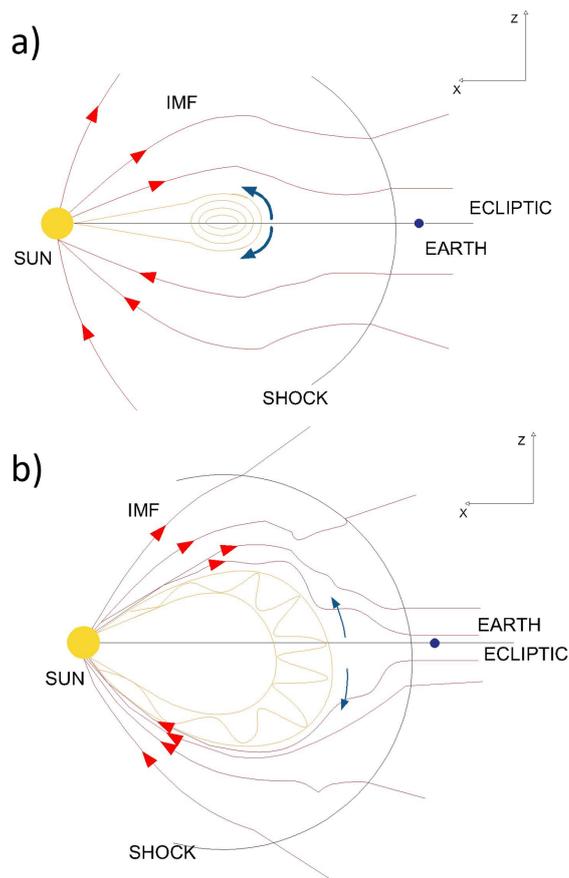
Fig. 1. Idealized IMF in the meridional plane, xz-plane of GSE coordinate system, and its interaction with embedded ICME with low inclination (upper panel) and high inclination (bottom panel). The NRF is shown with blue arrows where its width and length suggest the pronouncement of the plasma flows in front of the embedded ICME. The figure is adapted from Martinić et al. (2022).

eventually slides past the obstacle. This process should be more efficient for an ICME with a low inclination since the expansion in the xz-plane is smaller, and the ICME can push the draped field around the obstacle more easily than an ICME with high inclination.

Vandas et al. (1995) and Vandas et al. (1996) studied the propagation of two MCs, one low inclined and one high inclined, represented by Lundquist's cylindrical force-free solution (Lundquist 1950) in the inner heliosphere using the 2.5D MHD model. Details of this model can be found in Wu et al. (1979) (2D) and Wu et al. (1983) (2.5D). They found that the propagation of these MCs does not depend on the inclination of their axes with respect to the ecliptic plane (one lies in the ecliptic, and the other has an axis perpendicular to it). The MHD model used in these studies was confined to the solar equatorial plane and therefore does not provide a complete 3D MHD representation. In order to provide a better forecast of ICME arrivals, the influence of field line draping and associated nonradial flows (NRFs) on the ICME propagation from the observational perspective needs to be investigated on a statistically relevant sample of events. To our knowledge, this influence was first studied by observation in Martinić et al. (2022). In this present study, we extend the

data sample to provide better statistical coverage and investigate the effects of NRFs and field line draping on the propagation behavior of the CME. In Section 2, we describe the method by expanding on the study by Martinić et al. (2022). We highlight several dynamical features used to study the interaction between differently oriented ICMEs and the environment. In terms of the plasma flows in front of the ICME FR, we studied NRFs and shock orientation; and in terms of the overall drag, we studied drag parameter and ICME transit time. The main findings are presented in Section 3, and our conclusions are in Section 4.

2. Data and method

We searched for associated CME-ICME pairs from 1996 to 2020. The lists we used to create our sample can be found in the following studies: Nitta & Mulligan Skov 2017 (abbr. NM), Palmerio et al. 2018 (abbr. P), Temmer et al. 2021 (abbr. T), and Xie et al. 2021 (abbr. X).

In total, 113 CME-ICME pairs were found, but only 31 were used in our analysis. Most events were excluded for two reasons: insufficiently developed sheath region (32 excluded) and unclear MO boundary determination (30 excluded). The former relates to missing signatures of a clear sheath region ahead of the MO (for a discussion of CMEs with and without sheath regions, see Salman et al. 2020). As highlighted in Kilpua et al. (2017), the sheath thickness depends on the velocity and physical properties of the driving MO and the ambient solar wind, but sheath thickness has also been shown to increase from the nose toward the flanks. Unclear MO boundary determination is related to the subjectivity in determining the boundaries of the MO. There are some MO examples where there are clearly multiple rotations of the same or different magnetic field components, and in such cases, it is not straightforward to establish the MO boundaries and associate the example with a simple FR categorization of eight types. Other reasons why some of the events were excluded are as follows: faint CME front and multiple eruptions within the LASCO field of view (11 excluded); possible ICME interactions with other ICMEs or high-speed streams (4 excluded); no clear magnetic field rotation, that is ejecta-ICME, (1 excluded); no in situ data (1 excluded); possible incorrect CME-ICME association (1 excluded); and inconsistent dominant inclination derived from remote observations and in situ measurements (2 excluded). Ultimately, 31 CME-ICME pairs in the period from 1997 to 2018 with clear MO signatures were left.

2.1. Dominant inclination determination

We derived the dominant inclination for the CME-ICME pairs from both the remote and in situ data. For the remote data, we used SOHO/LASCO (Brueckner et al. 1995) coronagraph images and performed an ellipse fit. This method assumes that the outer edge of the (partial) halo CME can be represented by an ellipse whose major axis inclination indicates the dominant inclination of the CME. An example of the application of the ellipse-fitting technique to event number eight is shown in Figure 3. The top row shows running difference images in the LASCO-C2 and LASCO-C3 field of view (FOV). In the bottom row, the ellipse fitting is overlaid with a red line.

In situ data was obtained from the WIND and ACE space probes, available through the OMNI database (King & Papitashvili 2005). The dominant inclination from the in situ data was derived from the rotation of the magnetic field components in the MO part of the ICME using the GSE system. If the rotation of the B_z component was observed to change sign but the

B_y component retained its sign, we considered the event to be a dominantly low-inclined event (see Figure 2). On the other hand, if a sign change was observed in the B_y component but the B_z component remained the same throughout the MO, the event was considered to be dominantly high inclined. We divided all events into eight basic categories. Four of these eight categories are dominantly high inclined (ESW, ENW, WSE, and WNE), and the other four are dominantly low inclined (SWN, NWS, SEN, and SWN). Here, E stands for east, W for west, N for north, and S for south. The ESW type has an axis directed toward the south and a helical field rotating from east to west. The ENW type has the same helical field rotation, but the axial field is directed toward the north. The same applies to the others. The results of the classification are shown in Table 2.2. Al-Haddad et al. (2013) found that FR reconstruction shows different inclinations for different FR reconstruction techniques, and this varies greatly with the MO boundary set. This is the reason why we only distinguish between dominantly high- and dominantly low-inclined events, rather than deriving the exact inclination for each event (see Martinić et al. 2022).

In summary, we divided all events into two groups: events with predominantly low inclination and those with predominantly high inclination. Events with predominantly low inclination are those with an inclination of less than 40°, as determined from the ellipse fit, and with a rotation in the B_z magnetic field component (ESW, ENW, WSE, and WNE), as observed in situ. Events with predominantly high inclination are those with an inclination greater than 45°, as determined from the ellipse fit, and with rotation in the B_y magnetic field component (SWN, NWS, SEN, and NES), as seen in situ. We considered the events with an inclination between 40° and 45° to be intermediate inclination events and did not include them in the analysis.

For two CME-ICME pairs that were excluded, we found inconsistencies in the dominant inclination inferred from the in situ and remote data. Xie et al. (2021) showed that 25% of the events studied had a rotation of more than 40° from the near-Sun to L1. They also showed that 56% of these events exhibited rotation in the STEREO/SECCHI-COR2 FOV (i.e., in the mid-corona). Isavnin et al. (2013) showed that about one-third of the events studied showed a change in inclination from predominantly low to high, or vice versa. In our sample of 33 events, we found only two events where this was true. This could be due to the fact that we excluded over 30 CME-ICME pairs because of ambiguous rotation of the magnetic field components within the MO part of the ICME. Of the remaining 31 events, 19 are dominantly low inclined, while 12 are dominantly high inclined. These 31 CMEs are listed in Table 2.1, and their interplanetary counterparts, ICMEs, are listed in Table 2.2. The first column of Table 2.1 shows the event number accompanied by an abbreviation indicating which study the CME-ICME association was taken. The second column shows the first C2 appearance time as reported in the SOHO/LASCO CME catalog.[1] The third and fourth columns show the time at which the ellipse fit reconstruction was performed in the LASCO-C2 and LASCO-C3 FOV, respectively. This is followed by the columns showing the obtained tilt, in LASCO-C2 FOV and LASCO-C3 FOV, respectively. The last column shows whether the event is dominantly high or dominantly low inclined, as obtained from the ellipse fit in the LASCO-C2 and LASCO-C3 FOV. The letter "L" indicates that the event is dominantly low inclined and that the average of the absolute tilt values obtained from the ellipse fit reconstruction in LASCO-C2 and LASCO-C3 FOV is less than 40°. The

---

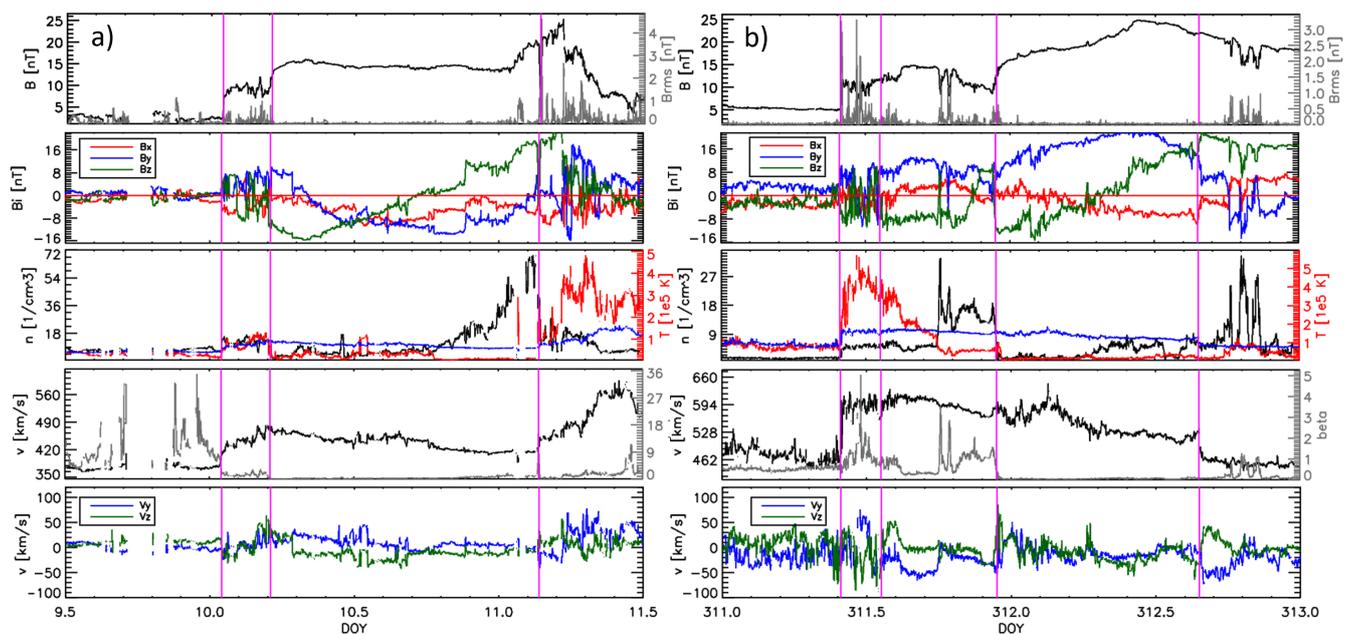[1] https://cdaw.gsfc.nasa.gov/CME_list/

Fig. 2. Interplanetary CME measured in situ on 10 January 1997 (left panels) and 3 November 2000 (right panels). From top to bottom, the following parameters are shown: Magnetic field magnitude in black and magnetic field fluctuations in gray (right scale); GSE magnetic field components (red, B_x; blue, B_y; green, B_z); proton density in black, temperature in red, and expected temperature in blue; solar wind speed in black and plasma beta parameter in gray; GSE velocity components (blue, B_y; green, B_z). From left to right, the vertical magenta lines mark the shock arrival, the end of the clear sheath, and the MO end time. In the right panels, the end of the clear sheath part does not coincide with the MO onset time, and there is an additional vertical magenta line present.
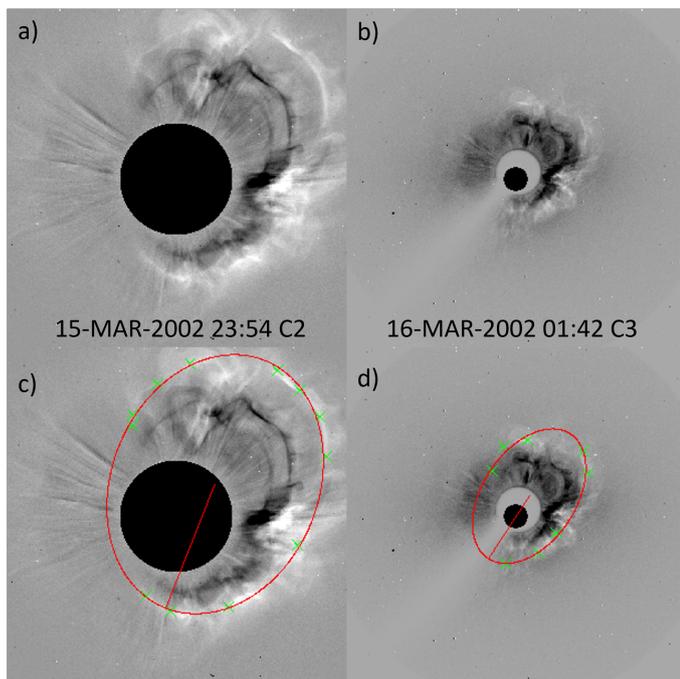

Fig. 3. Coronal mass ejection that occurred on 15 March 2002. The upper panels show the running difference images in LASCO-C2 (left) and LASCO-C3 (right). The bottom panels show the corresponding ellipse fitting. The ellipse is indicated with a red line, whereas green crosses mark the points outlined on the CME front used to obtain the fit.

letter "H" indicates that the event is dominantly high inclined. Analogously, such events are those whose average absolute tilt values are higher than 45°.

In Table 2.1, one can see that the inclination derived from LASCO-C2 may differ from the inclination derived from the LASCO-C3 coronagraphic images. The CME evolves through the entire FOV of C2 and C3, and by marking slightly different leading edges (green crosses in Figure 3) at different times, we can infer slightly different inclinations for the same event. We note that this is not necessarily related to strong rotations and deflections in the LASCO-C2 or LASCO-C3 FOV (Yurchyshyn et al. 2009; Vourlidas et al. 2011; Kay et al. 2017) but to simple ambiguities inherent in the measurements. This is also visible in Figure 3, where in LASCO-C3 FOV the ellipse is slightly less inclined than in the LASCO-C2 FOV. This is one of the reasons why we focus only on the dominant inclination.

2.2. Sheath region nonradial flows and shock orientation

The boundaries of the MO and sheath region were determined manually for each event. We note that the selection of ICME boundaries involves a degree of uncertainty. In the first instance, the boundaries of the MO were chosen to cover the entire magnetic field rotation. When this was not possible due to the rotation of several magnetic field components, the events were excluded. As mentioned earlier, there were 30 events where this was the case. From left to right, the columns in Table 2.2 show the event number, the date of the MO onset, shock-clear sheath occurrence time SH_{start}, clear sheath end time SH_{end}, the MO onset time, the MO end time, the derived FR type, the NRF ratio, the shock orientation θ_B, the observed transit time TT, and γ parameter. The sheath region was divided into two parts in some cases. The first part is the region where only clear sheath signatures can be seen (i.e., a strongly fluctuating magnetic field and plasma with increased density, temperature, and plasma beta). The second part of the envelope has fewer

Nr.	First C2 Appearance	Ellipse Fit in C2	Ellipse Fit in C3	Tilt C2 [°]	Tilt C3 [°]	Inclination
1[X]	1997-01-06 15:10	no data	1997-01-07 01:59		3	L
2[X]	1997-10-06 15:28	1997-10-06 18:44	1997-10-07 02:31	20	20	L
3[X]	1997-11-04 06:10	1997-11-04 06:42	1997-11-04 09:40	-87	74	H
4[X]	1998-01-02 23:28	1998-01-03 01:28	1998-01-03 03:40	-51	-89	H
5[X]	2000-08-09 16:30	2000-08-09 17:04	2000-08-09 21:18	33	30	L
6[X]	2000-11-03 18:26	2000-11-03 22:26	2000-11-04 01:42	-33	-27	L
7[X]	2001-04-26 12:30	2001-04-26 13:29	2001-04-26 14:15	35	8	L
8[X]	2002-03-15 23:00	2002-03-15 23:52	2002-03-16 01:42	71	67	H
9[X]	2002-04-15 03:50	2002-04-15 04:50	2002-04-15 05:18	21	24	L
10[X]	2003-08-14 20:06	2003-08-14 21:53	2003-08-15 02:40	55	50	H
11[X]	2005-05-13 17:12	2005-05-13 17:22	no data	54		H
12[T,X]	2008-12-12 08:54	2008-12-12 11:54	2008-12-12 15:42	-35	-37	L
13[T,X]	2010-04-03 10:33	2010-04-03 10:50	2010-04-03 12:42	6	-18	L
14[T,NM,X]	2010-06-16 14:54	2010-06-16 20:06	no data	-30		L
15[P,T,X]	2011-06-02 08:12	2011-06-02 08:48	2011-06-02 09:54	-57	-57	H
16[P,X]	2011-09-14 00:00	2011-09-14 01:36	2011-09-14 03:06	-15	-5	L
17[P,T,X]	2011-10-22 01:25	2011-10-22 02:24	2011-10-22 04:18	-53	-55	H
18[P,T]	2012-01-19 14:36	2012-01-19 15:48	2012-01-19 16:42	-2	-20	L
19[P,T,X]	2012-06-14 14:12	2012-06-14 14:36	2012-06-14 16:18	18	11	L
20[P,T,X]	2012-07-12 16:48	2012-07-12 17:24	no data	50		H
21[P,T,NM,X]	2012-10-05 02:48	2012-10-05 05:24	2012-10-05 08:42	45	45	H
22[T,X]	2012-11-09 15:12	2012-11-09 16:00	2012-11-09 18:20	31	22	L
23[P,X]	2013-01-13 12:00	2013-01-13 15:54	faint LE	-6	0	L
24[P,T,X]	2013-04-11 07:24	2013-04-11 08:24	2013-04-11 10:30	84	90	H
25[NM,X]	2013-06-23 22:36	2013-06-24 02:48	faint LE	59		H
26[P,T,X]	2013-07-09 15:12	2013-07-09 16:24	faint LE	12		L
27[P,T,X]	2014-08-15 17:48	2014-08-15 20:24	faint LE	-52		H
28[X]	2015-11-04 14:48	2015-11-04 15:24	2015-11-04 17:30	23	37	L
29[X]	2016-10-09 02:24	2016-10-09 06:24	2016-10-09 10:18	-15	-35	L
30[X]	2017-05-23 05:00	2017-05-23 08:24	2017-05-23 13:29	15	-3	L
31[X]	2018-03-06 01:25	2018-03-06 03:48	faint LE	20		L

Table 1. Remote features of the observed CMEs. The first column is the event number with the indication of where the CME-ICME association was taken from and is followed by the CME's first C2 appearance time. The third column corresponds to the time the ellipse fit was performed in LASCO-C2 FOV, and the fourth column is the time the ellipse fit was performed in LASCO-C3 FOV. The fifth and sixth columns show the tilt results derived from LASCO-C2 and LASCO-C3, respectively. The last column shows the dominant inclination obtained from Tilt C2 and Tilt C3 values (see text for details); "L" stands for low inclination, "H" stands for high inclination, and "LE" stands for the leading edge.

high plasma parameters and/or a not as strongly fluctuating magnetic field. This part shows no clear sheath and no clear MO properties. We identified this second part in 14 out of 31 events, as shown in Table 2.2 (see column SH_{end}). In these 14 events, the end of the clear sheath region does not correspond to the beginning of the MO part. This part between the clear sheath and the clear MO was studied by Kilpua et al. (2013), who recognized it as the disturbed front part of the FR known as the MO front region. More recently, Temmer & Bothmer (2022) recognized this as compressed ambient solar wind and noted it as a leading edge structure. An example of a sheath with clear sheath properties is shown in the left panels of Figure 2, while an example of a more complex sheath where the clear sheath is observed after the shock but then toward the MO part of the ICME one can also see a region with both sheath and MO properties is shown in the right panels of Figure 2. There, one can observe a region that shows a stronger magnetic field with fewer fluctuations than in the clear sheath part. The density and plasma beta parameter show a further increase accompanied by a decrease in the temperature.

Interplanetary CMEs are usually associated with NRFs in (1) the sheath region and (2) the expanding magnetic ejecta part. The first association is due to the plasma motion of the ambient solar wind escaping around the ICME ejecta part, and the second is related to the expansion of the magnetic ejecta in the nonradial direction, as described in Al-Haddad et al. (2022). The NRF in the sheath region was previously studied by Gosling & McComas (1987). They discovered a westward flow related to the magnetic stress of the Parker spiral acting on ICMEs. Later, Owens & Cargill (2004) showed that the NRF in the sheath region can be used as an indicator of the local axis orientation of ICMEs and the point at which spacecraft and ICMEs meet. Additionally, Liu et al. (2008) investigated whether NRFs in the sheath could relate to the curvature of the MO.

Similarly, Martinić et al. (2022) showed how differently oriented ICMEs may have different NRFs. We calculated the NRF ratio between the plasma flow in the y and z directions of the GSE coordinate system. The NRF flow is defined as the average of the absolute flow of the plasma in the y or z direction in GSE. The NRF ratio for each event is given in Table 2.2, column 8. We emphasize that the NRF ratio was determined from the part of the sheath where we observed only unique sheath features. For the 14 events mentioned above with complex sheath structures, this means that only the first part of the sheath was considered. In addition to the NRF in the sheath region, the shock orientation

Nr.	In Situ Date	SH_{start}	SH_{end}	MO_{start}	MO_{end}	FR type	NRF ratio	$\theta_B[°]$	TT[h]	$\gamma[10^{-7}\ km^{-1}]$
1	1997-01-10	10.04		10.21	11.14	SWN	0.56	51	46.46	0.096
2	1997-10-10	283.68	283.92	284.15	285	SWN	0.88	89	98.33	8.901
3	1997-11-07	310.95	311.26	311.68	312.57	WNE	1.85	no data	78.4	0.431
4	1998-01-07	6.58	6.98	7.11	8.4	ENW	1.28	59	90.31	0.418
5	2000-08-12	224.8		225.25	226.25	SEN	1.02	64	59.92	0.125
6	2000-11-06	311.4	311.55	311.95	312.65	SEN	1.06	46	68.3	1.141
7	2001-04-28	118.2	118.48	119.08	119.6	SEN	1	48	58.34	0.460
8	2002-03-19	77.55		78.24	79.52	WNE	0.96	39	75.59	0.355
9	2002-04-17	107.47	107.7	108.02	109.15	SWN	0.92	66	64.23	0.137
10	2003-08-18	229.58		230.12	231.25	ESW	1.13	62	53.9	2.332
11	2005-05-15	135.12	135.26	135.4	136.1	ENW	2.39	62	38.58	0.180
12	2008-12-17	351.5		352.2	352.8	NWS	1.22	no data	102.34	4.782
13	2010-04-05	95.35	95.48	95.53	96.57	NWS	0.43	54	45.31	
14	2010-06-21	171.95		172.35	173.7	NES	1.76	no data	99.07	4.169
15	2011-06-05	155.85		156.05	156.42	WNE	0.98	69	61.7	0.239
16	2011-09-17	260.15	260.35	260.69	261.49	SEN	1.02	87	80.39	0.227
17	2011-10-25	297.78	297.91	298.05	298.67	ENW	0.57	64	66.03	0.106
18	2012-01-22	22.25		22.52	22.77	NWS	0.87	85	66.73	0.465
19	2012-06-16	168.84	168.95	169.05	169.51	NES	1.76	60	55.95	0.135
20	2012-07-15	196.77		197.3	199.1	ESW	1.09	33	70.28	0.627
21	2012-10-08	282.22		282.76	283.35	ESW	1.84	74	81.32	0.502
22	2012-11-13	317.97		318.4	319.15	NES	0.66	68	84.6	0.276
23	2013-01-17	17		17.71	18.5	SWN	0.58	no data	88.54	7.762
24	2013-04-14	103.95		104.75	105.95	ENW	2.5	40	78.91	1.118
25	2013-06-28	178.6		179.1	180.5	WSE	2.23	74	88	0.831
26	2013-07-13	193.72		194.25	195.35	NWS	1.14	79	78.43	0.087
27	2014-08-19	231.28	231.77	231.9	233.48	WNE	1.2	85	90.06	
28	2015-11-07	310.75	311.08	311.3	312.48	SWN	0.82	46	59.28	0.222
29	2016-10-13	286.92		287.25	288.62	SEN	1.21	16	68.47	0.195
30	2017-05-28	147.65	147.9	147.98	149	SWN	1.33	81	101.1	0.065
31	2018-03-10	68.75		69	69.8	SWN	0.42	no data	54.89	0.164

Table 2. In-situ derived features of ICMEs, shock angle θ, and γ parameter obtained with the reverse modelling procedure. First column shows the event number. Next is the date of MO onset followed by sheath onset time (SH_{start}); sheath end time (SH_{end}); MO onset time (MO_{start}); and MO end time (MO_{end}), all given in day of the year (DOY). The following columns show the FR type, NRF ratio, shock orientation θ_B, observed transit time (TT) in hours. Finally, the gamma parameter is given in the last column.

θ_B, that is, the angle between the shock normal vector $\hat{n}$ and the upstream magnetic field B_{up}:

$$\theta_B = \frac{180°}{\pi} \arccos\left(\frac{|B_{up} \cdot \hat{n}|}{\|B_{up}\| \, \|\hat{n}\|}\right). \tag{1}$$

The shock normal vector $\hat{n}$ was calculated by the mixed-mode method Abraham-Shrauner & Yun (1976), and in the cases where the data gap of velocity components was present, magnetic coplanarity from Colburn & Sonett (1966) was used. (For more detail on the $\hat{n}$ calculation, we refer the reader to the database of interplanetary shocks from which the θ_B were obtained.[2]). The shock orientation θ_B values are given in Table 2.2. One can notice that not all events from Table 2.2 have a corresponding θ_B. These events (3, 12, 14, 23, and 31) do not meet the shock criterion given in the database of interplanetary shock documentation. However, they have a sheath developed enough to compute NRFs, as indicated above.

2.3. Transit time

The transit time (TT) was calculated as the time difference between the time of onset of the ICME MO in the in situ data and the CME start time at 20 R_s (solar radii). We note that this transit time is not the same as the one typically given in databases that corresponds to the arrival time of the shock. The CME start time at a starting radial distance of 20 R_s was taken from the second order fit of the altitude-time measurements provided by SOHO/LASCO CME catalog.[3] When measurements were only available for starting radial distances less than 20 R_s, an interpolation was performed using the acceleration corresponding to the same second order fit.

2.4. Drag-based model and γ parameter determination

Observational studies have derived that drag force dominates ICME propagation after a certain distance in the heliosphere. Results from these studies have formed the basis of numerous drag-based CME models (Vršnak et al. 2013; Hess & Zhang 2015; Möstl et al. 2015; Kay & Gopalswamy 2018), which apply the simple analytical equation:

$$F_d = \gamma(v - w)|v - w|, \tag{2}$$

where v is the CME velocity, w is the solar wind velocity, and γ is the so-called drag parameter given by the following equation (Vršnak et al. 2013):

---

[2] http://ipshocks.fi/database

[3] https://cdaw.gsfc.nasa.gov/CME_list/

$$\gamma = C_d \frac{A\rho_w}{M + M_V}. \tag{3}$$

Here, A is the cross-sectional area of the CME, ρ_w is the solar wind density, M is the CME mass, M_V is the mass corresponding to the volume of the fluid displaced by the movement of the body (the so-called virtual mass), and C_d is the dimensionless drag coefficient. We emphasize that C_d is usually taken as one and as a constant during the propagation of the ICME. However, Cargill (2004) has shown that the value of C_d depends on the relative density and velocity of the CME with respect to the density and velocity of the solar wind. Cargill also showed that the value of C_d increases from one for dense CMEs to as high as three for low-density CMEs and that C_d has a significant radial dependence for the latter.

The drag parameter γ is a very important parameter in the context of the drag force acting on a CME. Due to its dependence on CME cross section, mass, virtual mass, and solar wind density, obtaining the drag parameter γ through direct measurements is currently unreliable (see e.g. Vršnak et al. 2013; Dumbović et al. 2021). To derive the most reliable gamma value for our data sample, we used a reverse modeling method with the drag-based ensemble version v3 tool (DBEMv3 tool; Čalogović et al. 2021). In DBEMv3, input parameters (CME start time, CME source region longitude, CME half-width, solar wind speed, starting speed of CME, and γ parameter) with their uncertainties follow a normal distribution, with the observation input value set as the mean and three standard deviations as the uncertainty. The DBEMv3 tool creates 100,000 ensemble members from these input parameters and performs a single DBM run for each of them. For more detail on the creation of ensemble members using the DBEMv3 tool, the reader is referred to Čalogović et al. (2021), and for a comprehensive description of the basic DBM and later developed versions, such as this ensemble version, to Dumbović et al. (2021). The reverse modeling method with DBEM has also been used by Paouris et al. (2021) to find the optimal γ parameters and solar wind speed for a different subset of CME-ICME pairs.

For this particular study, the input parameters of CME start time, CME source region longitude, and CME half-width were set without uncertainties. These values are given in Table 3. The derivation of the CME start time is described in Sect. 2.3. The CME source region was determined from low coronal signatures: post-flare loops, coronal dimmings, sigmoids, flare ribbons, and filament eruptions. For this, we used the JHelioviewer (Müller et al. 2017) visualization tool. We analyzed 171, 211, 193, and 304 Å filtergrams from SDO/AIA (Lemen et al. 2012) and SDO/HMI (Scherrer et al. 2012) magnetogram data. When these data were not available, we used SOHO/EIT (Delaboudinière et al. 1995) and SOHO/MDI (Scherrer et al. 1995) magnetogram data. The CME half-width, λ, was set to 89° because all events were (partial) halo events as seen in the LASCO-C2 and LASCO-C3 FOV. The solar wind speed w and the starting speed of CME v_0 follow a normal distribution, with the mean value being an observed value given in Table 3. The solar wind speed was obtained from in situ plasma measurements provided by the OMNI database King & Papitashvili (2005), and it was determined as the mean velocity of the solar wind over an undisturbed period of several hours prior to the arrival of the CME shock. The CME start speed was taken as a second order speed given in SOHO/LASCO CME catalog.[4] The uncertainty (i.e., 3σ

---

[4] https://cdaw.gsfc.nasa.gov/CME_list/

---

value) for both the CME start speed and solar wind speed was set to 10% of the mean value. For the purpose of reverse modeling with DBEMv3, we set the allowed gamma range to 0.01-10 10^{-7} km^{-1} with an equal probability for all γ parameters in this range (i.e., the γ parameter followed a uniform distribution in this range). As part of the reverse modeling procedure, we searched for the optimal γ parameters where the forecast transit time is within one hour of the actual observed transit time. The median values of these obtained γ parameters are listed in Table 2.2.

Events 1, 10, 26, 27, 29, and 31 in Table 3 are marked with an asterisk. For these events, the original DBEMv3 input was changed because there were no transit times matching the observed transit time within one hour (i.e., no γ parameters were found). We studied those events in more detail, and we found that for events 1, 10, 29, and 31, the radial takeoff distance needed to be changed. For events 26 and 27, the takeoff speed and speed uncertainty needed to be increased.

The height at which the drag force begins to dominate is not universal and varies greatly from event to event (Vršnak 2001; Sachdeva et al. 2015; Sachdeva et al. 2017). For events 1, 10, 29, and 31, we found that a starting radial distance of $20R_s$ is not suitable as a DBEM input because the CME is still accelerating at this distance, and its propagation is therefore not dominated by the drag force. To improve our input for these events, the starting distance was increased by the trial-and-error method until a suitable initial distance was found that provided a "perfect transit time" (similar to Sachdeva et al. 2015). For events 1, 10, and 31, this distance was found to be 70 R_s, and we found it to be 50 R_s for event 29.

For events 26 and 27, we found that the initial CME speed at 20 R_s may be underestimated. This speed underestimation might come from the use of the second order fit of the height-time measurements. The second order fit shows a very small deceleration in the LASCO FOV. A linear fit yielded slightly different velocity estimates that provided physical solutions to find an optimal γ with DBEM for event 26. The uncertainties of the CME launch speed were also increased to 20% in order to better compensate for the initial underestimation of velocity. For event 27, even after considering the linear speed and after increasing the uncertainties of the initial velocity, the optimal γ parameter was not found. It could be that the DBM does not capture the physics of this event well. The same is true for event 13. This CME was launched on 3 April 2010 and is a well-studied event (Rodari et al. 2018; Zhou et al. 2014; Rollett et al. 2012; Temmer et al. 2011; Liu et al. 2011). Temmer et al. (2011) reported quite complex CME dynamics in the LASCO FOV and later in the heliosphere. This CME initially strongly accelerated up to 1100 km s^{-1} and then had an abrupt deceleration down to 800 km s^{-1} (all below 20 R_s). Later, the CME again accelerated and decelerated in the heliosphere, possibly due to a high-speed stream crossing. Due to its complex dynamics, this event is not suitable for reverse modeling with the DBEM or DBM in general. We find that it is also important to emphasize that even more sophisticated 3D MHD models such as ENLIL were not able to correctly represent the propagation of this CME (Temmer et al. 2011).

We note that some of the obtained γ values lay outside of an expected range, 0.2-2 10^{-7} km^{-1}, as given by Vršnak et al. (2013). This is most prominent for events 2, 12, 14, and 23 (see Table 2.2). We also emphasize that such high γ values might be unreal, but testing such an assumption is beyond the scope of this paper. This would require meticulous analysis of the pre-eruption state of the heliosphere as well as detailed eruption analysis (see Žic et al. 2015 and Temmer et al. 2012). We also

Nr.	t_0	v_0 [kms^{-1}]	ϕ_{CME} [°]	w [kms^{-1}]
1*	1997-01-08 06:34	625	6	375
2	1997-10-07 01:16	620	0	407
3	1997-11-04 09:55	700	25	335
4	1998-01-03 08:20	515	40	309
5	2000-08-09 21:05	720	-15	416
6	2000-11-04 02:30	643	0	475
7	2001-04-26 15:35	1084	20	444
8	2002-03-16 02:10	917	7	293
9	2002-04-15 08:15	731	7	331
10*	2003-08-15 15:14	630	0	471
11	2005-05-13 19:00	1689	0	415
12	2008-12-12 20:47	432	-10	339
13	2010-04-03 15:10	661	20	509
14	2010-06-17 05:20	397	2	370
15	2011-06-02 11:30	996	6	337
16	2011-09-14 08:10	457	7	413
17	2011-10-22 07:10	663	25	323
18	2012-01-19 17:45	1390	-24	326
19	2012-06-14 17:15	983	-7	297
20	2012-07-12 18:55	2265	-20	326
21	2012-10-05 08:55	804	15	318
22	2012-11-09 21:00	603	-20	284
23	2013-01-14 00:33	339	-22	403
24	2013-04-11 11:05	819	-15	390
25	2013-06-24 10:10	513	40	373
26*	2013-07-09 23:34	450	-20	386
27*	2014-08-16 03:00	342	5	295
28	2015-11-04 19:55	708	5	465
29*	2016-10-10 09:31	495	-17	355
30	2017-05-23 16:30	367	0	303
31*	2018-03-07 17:06	538	-8	366

Table 3. DBEM input parameters. The number of the CME is indicated under Nr.; t_0 is the CME start date and time in UT at 20 R_{SUN}; v_0 is the CME start speed at 20 R_{SUN} given in km s^{-1}; ϕ_{CME} is the longitude of the CME source position in degrees; and w is the solar wind speed in km s^{-1}.

highlight that from a theoretical point of view (see Equation 2), for cases when the CME launch speed is close to the solar wind speed, the corresponding optimal γ obtained by the reverse modeling with drag-based models can easily take on very large values that may not be physically plausible. However, we also note that the reverse modeling procedure gave results close to the expected range of values for the majority of events, (i.e., for 25 out of 31 events).

3. Results and discussion

Dominant inclination results obtained from remote and in situ data are given in the last column of Table 2.1 and the sixth column of Table 2.2, respectively. In Figure 4, we show the occurrence frequency of dominantly low- and high-inclined events with respect to NRF, transit time, shock orientation, and γ parameter. One can see that most of the high- and low-inclination events have NRF ratios close to one. However, there is a greater number of low-inclination events with low NRF ratios and a greater number of high-inclination events with high NRF ratios. This is consistent with the results of Martinić et al. (2022), where a similar procedure was applied to a smaller sample of events. This suggests that NRFs are more pronounced in the $\pm y$ direction for events with high inclination and in the $\pm z$ direction for

events with low inclination. The mean, median, standard deviation, and 95th percentile for NRF ratios are shown in Table 3. The mean, median, and 95th percentile show larger values for high-inclination events, confirming the results of the distribution plot in panel (a) of Figure 4. We observed that the standard deviation for high-inclination events is almost twice the standard deviation of low-inclination events, which is related to the spread of NRF values. Namely, low-inclination events can be found in the 95th percentile interval [0.42, 1.76], while high-inclination events have a 95th percentile interval [0.78, 2.44].

As stated earlier, the NRF ratios were calculated from the velocity in the y and z directions of the GSE coordinate system in the clear sheath part of the ICME and are a consequence of ambient plasma interacting with the FR part of the ICME. However, we note that the deflection of plasma due to fast-forward shock may also contribute to the NRF and this contribution cannot be easily disentangled from the contribution due to draping. In order to confirm that the above-stated dependence of NRF ratios on ICME inclination comes from plasma being deflected around the ICME FR part rather than from plasma that is being deflected on the shock front, we calculated the shock orientation and studied the dependence of shock orientation on inclination. This dependence can be seen in the distribution of θ_B in panel (c) of Figure 4. Unlike NRF ratios, the shock orientation (which determines the shocked plasma deflection right behind the shock front) does not show dependence on ICME inclination. From Table 2.2, we also observed that most events have θ_B greater than 45°, which means that most of the events studied have a quasi-perpendicular shock front.

In order to quantitatively test the difference between low- and high-inclination samples, we performed the Welch's test (in case of different sample variances) and the student t-test (in case of similar sample variances). First, in order to choose an adequate test for the means of the populations, we had to test the sample variances. To see whether two samples have similar or different variances we used a statistical F-test. According to the F-test, with a 95% confidence level, the shock orientation θ_B and transit time have similar variances for high- and low-inclination groups of events; however, for NRF ratio and gamma parameter γ, these two groups of events show statistically significant variances. High-inclination events (orange bars in Figure 4) have a wider spread in NRF ratios in comparison to low-inclination events (blue bars), shifting the distribution toward higher NRF ratio values. Regarding the γ parameter, low-inclination events (blue bars in Figure 4, panel d) have a wider spread. The same is not valid for transit time and shock orientation.

Welch's test null hypothesis is that the NRF ratios for low- and high-inclination events come from random samples from normal distributions with equal means and unequal variances. Welch's test was performed under the assumption that (1) the NRF ratio/ γ parameter for high- and low-inclination events are independent, (2) the NRF ratio/ γ parameter distributions for low- and high-inclination samples are normal, and (3) the NRF ratio/ γ parameter variances for low-inclination and high-inclination events are different (according to the F-test).

The result of Welch's test for NRF ratios is that the null hypothesis should be rejected at the 95% significance level (i.e., the NRF ratios for high- and low-inclination events come from populations with unequal means). The interpretation of the different NRFs observed for ICMEs with different inclinations comes from the fact that the ambient plasma in front of the ICME bypasses the obstacle (ICME FR) in a way where the extent of the obstacle is smaller. For ICMEs with low inclination, the extent of the ICME FR part in the $\pm z$ direction is smaller than in the $\pm y$
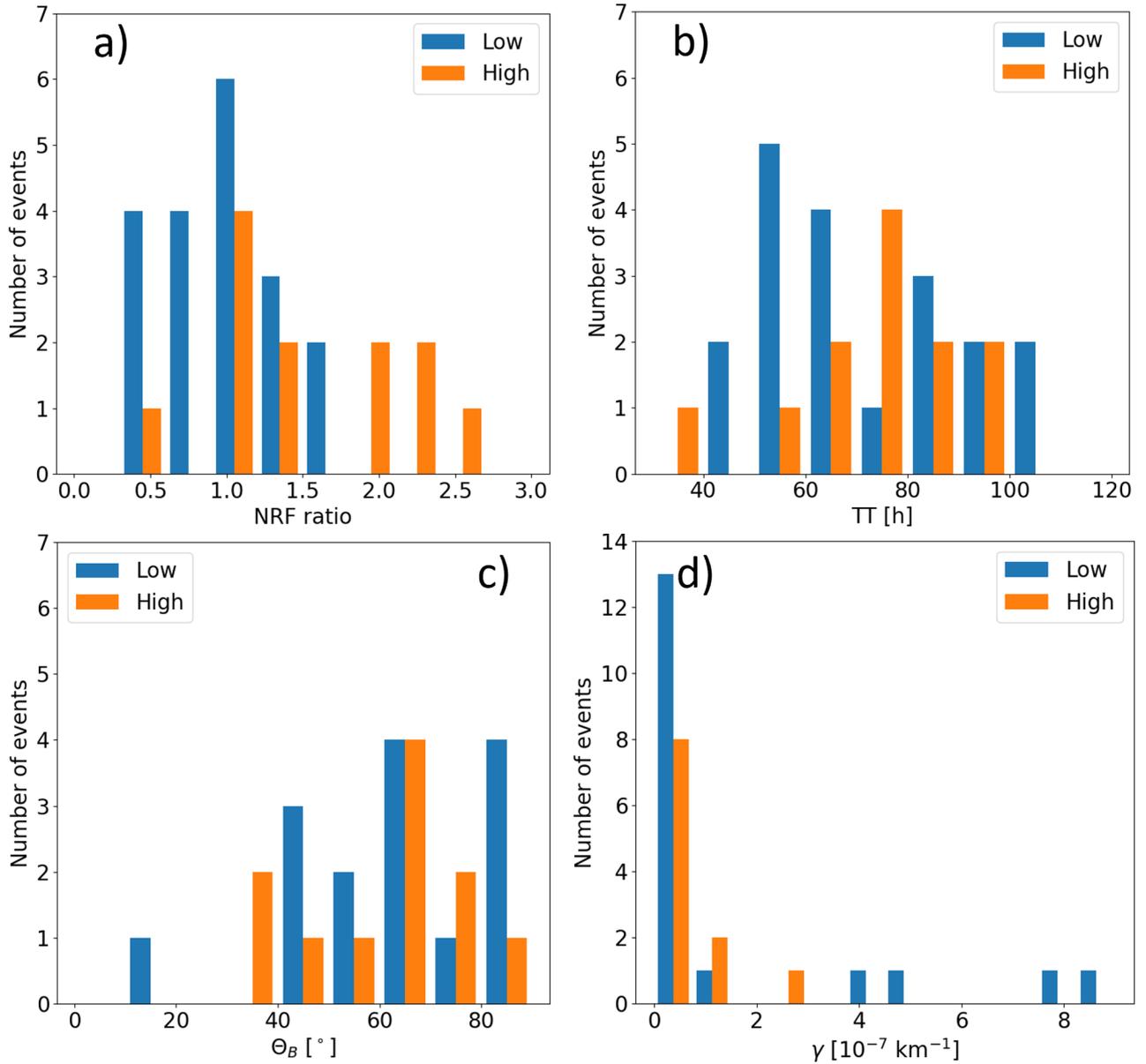
Fig. 4. Distributions for NRF ratio, transit time (TT), shock orientation (θ_B), and drag parameter γ for high-inclination events (orange) and low-inclination events (blue).

Table 4. Statistical results. Mmean, median, standard deviation, and 5. and 95. percentiles for low- and high-inclination events (reported separately).

	LOW INCLINATION				HIGH INCLINATION			
	NRF ratio	$\theta_B[°]$	TT[h]	$\gamma[\times 10^{-7} km^{-1}]$	NRF ratio	$\theta_B[°]$	TT[h]	$\gamma[\times 10^{-7} km^{-1}]$
MEAN	0.98	62.67	72.7	1.63	1.5	60.09	72.8	0.65
MEDIAN	1.00	64	68.3	0.22	1.24	62	76.99	0.43
STD	0.37	19.31	18.63	2.80	0.61	15.64	15.02	0.60
PERC[5,95]	[0.42,1.76]	[37,87.6]	[46.35,101.22]	[0.08,7.93]	[0.78,2.44]	[36,79.5]	[47.00,90.44]	[0.14,1.72]

direction, and therefore the NRF ratio is smaller for ICMEs with low inclination. In contrast, the extent of the ICME with high inclination is smaller in the $\pm y$ direction, so the plasma flows mainly in this direction. A sketch of the various NRFs in terms of the different inclinations of CMEs is shown in Martinić et al. (2022). The result of Welch's test for the γ parameter is that the null hypothesis should not be rejected (i.e., the γ parame-

ter for high- and low-inclination events comes from populations with equal means). Welch's test is based on the normality assumption, which is hardly satisfied for γ values (see histogram in Figure 4, panel d). The Kolmogorov-Smirnov test and Mann-Whitney U-test, as nonparametric significance tests, were also performed. However, we note that both tests confirmed the results from Welch's test at the same confidence interval (95%),

meaning that there is no significant difference between low- and high-inclination events regarding γ values.

For shock orientation and transit time, the F-test confirmed similar variances for low- and high-inclination samples. Thus, instead of Welch's test, the student t-test was performed under the assumption that (1) the shock orientation/transit time for high- and low-inclination events are independent, (2) the shock orientation/transit time distributions for low- and high-inclination samples are normal, and (3) the shock orientation/transit time variances for low-inclination and high-inclination events are similar (according to the F-test).

The t-test confirmed the null hypothesis at the 95% significance level, meaning that the samples of shock inclination and transit time for low- and high-inclination events come from populations with equal means. In other words, there is no statistically significant difference between low- and high-inclination groups of events.

The fact that there is no difference in the γ parameter and transit time for differently oriented CMEs suggests that the orientation of the CME does not affect the overall drag of the CME. However, we note that the drag depends primarily on the difference between the velocity of the CME and the ambient solar wind speed. In addition, the γ parameter depends on the CME cross section, the ambient solar wind density, the mass of the CME, and the virtual mass. It is possible that the effect of inclination is small enough to be "masked" by all these contributions, even though we selected the sample in order to minimize them. As described in Martinić et al. (2022), the inclination effect on the drag should be most pronounced at the minimum of the solar cycle, where the configuration of the IMF most closely matches that of a simple magnetic dipole. While our sample of events includes some that occurred near the minimum of solar activity (event numbers 11,12,13,14, and 31), the majority of events correspond to the maximum, when the IMF configuration is very complex. Due to the very small sample of events at the minimum of solar activity, no analysis of the difference between events at the minimum and maximum of activity was performed.

Except for inclination influence, Vandas et al. (1995) and Vandas et al. (1996) also emphasized the importance of the chirality of the CME for its propagation, which is not captured by our study. This was later tackled by Chané et al. (2006), who studied the propagation of two CMEs: one in which the initial magnetic field and the background magnetic field had the same polarity and another where they had opposite polarities. Their simulations showed that the initial magnetic polarity significantly affects the evolution of CMEs. We note here that the study of Chané et al. (2006) did not examine the effects of CME inclination but rather the effects of initial chirality on propagation in the inner heliosphere. More recently, Shen et al. (2021) studied the effects of different initial CME densities, masses, sizes, and magnetic field configurations on simulation results for observers near Earth and Mars. Nevertheless, to our knowledge, there are no 3D MHD studies aimed specifically at investigating the effects of (I)CME inclination and its interaction with the environment, such as IMF draping and plasma flows ahead of the ICME. Such a study could beneficially complement our findings based on observations.

4. Summary and conclusions

Altogether, 31 Earth-directed CME-ICME pairs with distinct magnetic obstacle (MO) properties and pronounced sheath regions during the period from 1997 to 2018 were studied. We inferred the dominant inclination from the ellipse fitting of LASCO-C2 and LASCO-C3 coronagraphic images. The dominant inclination was also derived from in situ data of the rotation of magnetic field components in the MO part of the ICME. Of the 31 CME-ICME pairs, 19 are low-inclination events, and 12 are high-inclination events.

Some basic features of the ICME propagation in terms of the inclination of the event were analyzed. We investigated the NRFs in the sheath region along with the shock orientation, transit time, and γ parameter. We found a significant difference in NRFs for differently oriented ICMEs. Low-inclination events were found to have lower NFR ratios, while high-inclination events were found to have higher NFR ratios. This implies that low-inclination events are more likely to have ambient plasma escape via the meridional plane, while high-inclination events are more likely to have plasma escape via the ecliptic plane (see Martinić et al. 2022).

The plasma deflection on the fast-forward shock could also contribute to the measured NRF ratios. To confirm that the above-stated difference between low- and high-inclination events is indeed due to the deflection of the plasma around the obstacle (ICME FR part) and not due to the deflection of the plasma by the shock front, we examined the dependence of the NRF ratios on the shock orientation. We found no differences in the NRF occurrence frequency with respect to the shock orientation, thus confirming the result stated above.

No significant difference was found in the transit time and γ parameter for differently oriented ICMEs. This suggests that the predominant inclination of the ICME has no effect on the drag due to the interaction with the ambient solar wind and IMF. We note that by inclination we mean tilt, that is, the angle between the elliptic plane and ICME flux rope axis, not the magnetic field orientation. We also emphasize that most of the studied events occurred near solar maximum, which is when the IMF has a very complex configuration. It is also possible that the influence of the inclination on the drag force is much smaller than the contributions of other features, such as the difference between the speed of the CME and the solar wind, the CME mass, the CME cross section, and the ambient density, and therefore the inclination effect is very difficult to decipher.

References

Abraham-Shrauner, B. & Yun, S. H. 1976, J. Geophys. Res., 81, 2097

Al-Haddad, N., Galvin, A. B., Lugaz, N., Farrugia, C. J., & Yu, W. 2022, ApJ, 927, 68

Al-Haddad, N., Nieves-Chinchilla, T., Savani, N. P., et al. 2013, Sol. Phys., 284, 129

Bothmer, V. & Schwenn, R. 1998, Annales Geophysicae, 16, 1

Brueckner, G. E., Howard, R. A., Koomen, M. J., et al. 1995, Sol. Phys., 162, 357

Burlaga, L. F. E. 1991, Magnetic Clouds, 152

Byrne, J. P., Gallagher, P. T., McAteer, R. T. J., & Young, C. A. 2009, A&A, 495, 325

Cargill, P. J. 2004, Sol. Phys., 221, 135

Cargill, P. J., Chen, J., Spicer, D. S., & Zalesak, S. T. 1996, J. Geophys. Res., 101, 4855

Chané, E., van der Holst, B., Jacobs, C., Poedts, S., & Kimpe, D. 2006, A&A, 447, 727

Chen, J. 1996, J. Geophys. Res., 101, 27499

Chen, J., Howard, R. A., Brueckner, G. E., et al. 1997, ApJ, 490, L191

Colburn, D. S. & Sonett, C. P. 1966, Space Sci. Rev., 5, 439

Delaboudinière, J. P., Artzner, G. E., Brunaud, J., et al. 1995, Sol. Phys., 162, 291

Dumbović, M., Čalogović, J., Martinić, K., et al. 2021, Frontiers in Astronomy and Space Sciences, 8, 58

Gopalswamy, N., Lara, A., Lepping, R. P., et al. 2000, Geophys. Res. Lett., 27, 145

Gosling, J. T. & McComas, D. J. 1987, Geophys. Res. Lett., 14, 355

Hess, P. & Zhang, J. 2015, ApJ, 812, 144

Isavnin, A., Vourlidas, A., & Kilpua, E. K. J. 2013, Sol. Phys., 284, 203

Kay, C. & Gopalswamy, N. 2018, Journal of Geophysical Research (Space Physics), 123, 7220

Kay, C., Gopalswamy, N., Xie, H., & Yashiro, S. 2017, Sol. Phys., 292, 78

Kilpua, E., Koskinen, H. E. J., & Pulkkinen, T. I. 2017, Living Reviews in Solar Physics, 14, 5

Kilpua, E. K. J., Isavnin, D., Vourlidas, A., Koskinen, H. E. J., & Rodriquez, L. 2013, Annales Geophysicae, 31, 1251

King, J. H. & Papitashvili, N. E. 2005, Journal of Geophysical Research (Space Physics), 110, A02104

Krall, J. & St. Cyr, O. C. 2006, ApJ, 652, 1740

Lemen, J. R., Title, A. M., Akin, D. J., et al. 2012, Sol. Phys., 275, 17

Liu, Y., Luhmann, J. G., Bale, S. D., & Lin, R. P. 2011, ApJ, 734, 84

Liu, Y., Manchester, W. B., Richardson, J. D., et al. 2008, Journal of Geophysical Research (Space Physics), 113, A00B03

Lundquist, S. 1950, Ark. Fys

Manoharan, P. K. 2006, Sol. Phys., 235, 345

Martinić, K., Dumbović, M., Temmer, M., Veronig, A., & Vršnak, B. 2022, A&A, 661, A155

McComas, D. J., Gosling, J. T., Bame, S. J., Smith, E. J., & Cane, H. V. 1989, J. Geophys. Res., 94, 1465

McComas, D. J., Gosling, J. T., Winterhalter, D., & Smith, E. J. 1988, J. Geophys. Res., 93, 2519

Moore, R. L., Sterling, A. C., Hudson, H. S., & Lemen, J. R. 2001, ApJ, 552, 833

Möstl, C., Rollett, T., Frahm, R. A., et al. 2015, Nature Communications, 6, 7135

Müller, D., Nicula, B., Felix, S., et al. 2017, A&A, 606, A10

Mulligan, T., Russell, C. T., & Luhmann, J. G. 1998, Geophys. Res. Lett., 25, 2959

Nitta, N. & Mulligan Skov, T. 2017, in AGU Fall Meeting Abstracts, Vol. 2017, SH51E–04

Owens, M. & Cargill, P. 2004, Annales Geophysicae, 22, 4397

Palmerio, E., Kilpua, E. K. J., Möstl, C., et al. 2018, Space Weather, 16, 442

Paouris, E., Čalogović, J., Dumbović, M., et al. 2021, Sol. Phys., 296, 12

Rodari, M., Dumbović, M., Temmer, M., Holzknecht, L., & Veronig, A. 2018, Central European Astrophysical Bulletin, 42, 11

Rollett, T., Möstl, C., Temmer, M., et al. 2012, Sol. Phys., 276, 293

Sachdeva, N., Subramanian, P., Colaninno, R., & Vourlidas, A. 2015, ApJ, 809, 158

Sachdeva, N., Subramanian, P., Vourlidas, A., & Bothmer, V. 2017, Sol. Phys., 292, 118

Salman, T. M., Lugaz, N., Farrugia, C. J., et al. 2020, ApJ, 904, 177

Scherrer, P. H., Bogart, R. S., Bush, R. I., et al. 1995, Sol. Phys., 162, 129

Scherrer, P. H., Schou, J., Bush, R. I., et al. 2012, Sol. Phys., 275, 207

Sheeley, N. R., Walters, J. H., Wang, Y. M., & Howard, R. A. 1999, J. Geophys. Res., 104, 24739

Shen, F., Liu, Y., & Yang, Y. 2021, ApJS, 253, 12

Siscoe, G. & Odstrcil, D. 2008, Journal of Geophysical Research (Space Physics), 113, A00B07

Temmer, M. & Bothmer, V. 2022, A&A, 665, A70

Temmer, M., Holzknecht, L., Dumbović, M., et al. 2021, Journal of Geophysical Research (Space Physics), 126, e28380

Temmer, M., Rollett, T., Möstl, C., et al. 2011, ApJ, 743, 101

Temmer, M., Vršnak, B., Rollett, T., et al. 2012, ApJ, 749, 57

Thernisien, A. F. R., Howard, R. A., & Vourlidas, A. 2006, ApJ, 652, 763

Vandas, M., Fischer, S., Dryer, M., Smith, Z., & Detman, T. 1995, J. Geophys. Res., 100, 12285

Vandas, M., Fischer, S., Dryer, M., Smith, Z., & Detman, T. 1996, J. Geophys. Res., 101, 2505

Čalogović, J., Dumbović, M., Sudar, D., et al. 2021, Sol. Phys., 296, 114

Vourlidas, A., Colaninno, R., Nieves-Chinchilla, T., & Stenborg, G. 2011, ApJ, 733, L23

Vršnak, B. 2001, Sol. Phys., 202, 173

Vršnak, B., Ruždjak, D., Sudar, D., & Gopalswamy, N. 2004, A&A, 423, 717

Vršnak, B., Žic, T., Vrbanec, D., et al. 2013, Sol. Phys., 285, 295

Žic, T., Vršnak, B., & Temmer, M. 2015, ApJS, 218, 32

Wu, S. T., Dryer, M., & Han, S. M. 1983, Sol. Phys., 84, 395

Wu, S. T., Han, S. M., & Dryer, M. 1979, Planet. Space Sci., 27, 255

Xie, H., Gopalswamy, N., & Akiyama, S. 2021, ApJ, 922, 64

Yurchyshyn, V., Abramenko, V., & Tripathi, D. 2009, ApJ, 705, 426

Zhou, Y., Feng, X., & Zhao, X. 2014, Journal of Geophysical Research (Space Physics), 119, 9321